Original Research Article

International journal of spray and combustion dynamics

International Journal of Spray and Combustion Dynamics
2018, Vol. 10(2) 111–130

DOI: 10.1177/1756827717738139
journals.sagepub.com/home/scd
SAGE

Modelling the generation of temperature inhomogeneities by a premixed flame

Thomas Steinbacher, Max Meindl and Wolfgang Polifke

Abstract

The response of a laminar, premixed flame to perturbations of upstream equivalence ratio is investigated and modelled, with emphasis on the generation of 'entropy waves', i.e. entropic inhomogeneities of downstream temperature. Transient computational fluid dynamics simulations of two adiabatic lean methane-air flames of different Péclet numbers provide guidance and validation data for subsequent modelling. The respective entropy transfer functions, which describe the production of temperature inhomogeneities, as well as transfer functions for the variation of the heat release, are determined from the computational fluid dynamics time series data by means of system identification. The processes governing the dynamics of the entropy transfer functions are segregated into two sub-problems: (1) heat release due to chemical reaction at the flame front and (2) advective and diffusive transport. By adopting a formulation in terms of a mixture fraction variable, these two sub-problems can be treated independently from each other. Models for both phenomena are derived and analysed using simple 0- and 1-dimensional configurations. The heat release process (1) is represented by a fast-reaction-zone model, which takes into account variations of the specific heat capacity with equivalence ratio in order to evaluate the magnitude of downstream temperature fluctuations with quantitative accuracy. For the transport processes (2), two types of models based on mean field data from the computational fluid dynamics simulation are proposed: A semi-analytical, low-order formulation based on stream lines, and a state-space formulation, which is constructed by Finite Elements discretisation of the transport equation for mixture fraction. Model predictions for the entropy transfer functions are found to agree well with the computational fluid dynamics reference data at very low computational costs.

Keywords

Entropy waves, hot spots, entropy transfer function, flame response, premixed combustion, secondary combustion noise, advective dispersion

Date received: 11 May 2017; accepted: 25 September 2017

1. Introduction

Modern low-emission gas turbines are prone to self-excited thermoacoustic instabilities, which arise from feedback between the combustion process and the acoustics inside the combustor. They can lead to high amplitude pressure oscillations, which might in extreme cases even cause system failure.[1–3] For stable configurations, thermoacoustic feedback may affect the emission of broad-band combustion noise from turbulent flames.[2,4–6] Thus, studies of combustion noise and thermoacoustic combustion instability are both linked to the study of thermoacoustic feedback mechanisms, which are outlined in the following.

Technically premixed flames, i.e. flames operated with a temporally fluctuating and spatially non-uniform equivalence ratio that result from imperfect, unsteady mixing of fuel and air, are subjected to perturbations of velocity u' and equivalence ratio ϕ', as illustrated in Figure 1. These disturbances lead to (1) changes of the heat release rate of the flame and (2), eventually, to the generation of temperature inhomogeneities T' in the exhaust gases (oval regions in Figure 1), which are often called 'hot spots' or 'entropy waves'. Effect (1) leads directly to the generation of

Fakultät für Maschinenwesen, Technische Universität München, Garching, Germany

Corresponding author:
Thomas Steinbacher, Technische Universität München, Fakultät für Maschinenwesen, Boltzmannstr. 15, Garching 85747, Germany.
Email: steinbacher@tfd.mw.tum.de

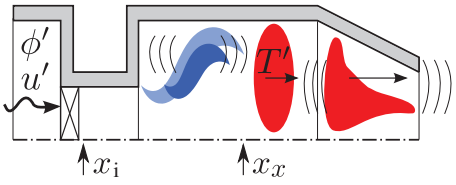

Figure 1. Sketch of the generation of primary and secondary combustion noise inside a combustor which is exposed to velocity and equivalence ratio fluctuations.

sound and, hence, noise produced by this mechanism is referred to as 'direct combustion noise'.[5,7] Hot spots originating from process (2) are convected downstream, where they are accelerated due to the presence of a nozzle. This leads to generation of sound that is only indirectly related to unsteady combustion.[8,9] Thus, noise emissions that can be related to these interactions are referred to as 'indirect combustion noise'.[10,11] Moreover, compositional inhomogeneities[12,13] and fluctuations in vorticity[14,15] may also contribute to the generation of indirect noise. In the following, we limit ourselves to entropic, i.e. temperature-related, fluctuations.

Acoustic perturbations generated by an entropy wave at the combustor exit nozzle will propagate back to the flame and the burner, which results in a modulation of equivalence ratio upstream of the flame and hence its heat release rate. These processes constitute an additional feedback loop, which will contribute to thermoacoustic interactions. In particular, interactions that involve entropy waves may lead to low-frequency thermoacoustic instabilities ('rumble'), or influence stability margins or amplitude levels of instabilities that are related to cavity acoustic modes.[16–20] For sequential combustors, an additional effect not related to a feedback has to be considered: Temperature fluctuations generated by the first stage have a strong impact on the second stage combustion process. Hence, they play a decisive role for the generation of noise and system stability.[21] Consequently, precise models for the prediction of hot spots emitted by the first stage are particularly desired for this type of combustion systems.

Interest in indirect combustion noise and thermoacoustic instabilities related to entropy waves has grown in recent years, as reviewed by Morgans and Duran.[11] However, the generation of temperature inhomogeneities by the flame has not been given much attention. Early studies employed simplistic models for the generation of entropy waves from inhomogeneities of equivalence ratio.[16–18] Many studies on the influence of the entropy feedback on noise or system stability relate downstream temperature fluctuations in a direct manner to the global heat release rate.[10,20,22,23] However, Strobio-Chen et al.[24] demonstrated that simply equating fluctuations of heat release rate of a premixed flame with the rate of generation of entropy waves can lead to invalid conclusions. They further showed that perturbations of equivalence ratio are the dominant mechanism of entropy wave generation in technically premixed flames. The analytical results were confirmed by a computational fluid dynamics (CFD) study on a laminar flame.[25] Wassmer et al.[26] recently presented more detailed measurement data and a low-order model for the flame response to upstream equivalence ratio fluctuations.

The goal of the present study is to develop a method for the quantitative prediction of entropy waves, i.e. temperature fluctuations, downstream a perturbed premixed flame from stationary flow field data. The paper is organised as follows: In section 2, the conceptual background is clarified and the response of flames to fluctuations in equivalence ratio is theoretically discussed. In section 3, the generation of temperature inhomogeneities is numerically analysed using two test setups. Steady state CFD results are shown and transfer functions identified with a CFD/system identification (SI) approach[27] – i.e. the post-processing of CFD time series data with SI – are presented. These results serve as a validation basis for the modelling concepts that are developed in the remaining parts of the paper. In section 4, a modelling concept for the transformation of equivalence ratio to temperature fluctuations by the combustion process is introduced. It focuses solely on this transformation and neglects convective transport processes before and after the flame. Two variants of a model of the transport processes are provided in section 5: a semi-analytical one using CFD streamline data (section 5.2) and a numerical one using CFD field data (section 5.3). For the sake of clarity, the basic concepts of both models are introduced by simple one-dimensional (1D) considerations in section 5.1. Overall models for the entropy transfer function (ETF) are constructed as a combination of the combustion model described in section 4 and one of the transport models described in section 5. They are validated against the CFD/SI results in section 6. Finally, the expected range of validity of the proposed modelling concepts is discussed in section 7.

2. Conceptual background

In this section, we first clarify the use of the terms entropy and temperature fluctuations throughout the paper. Then, the physical mechanisms which lead to the generation of entropy fluctuations downstream a flame are discussed with the help of an illustrative example. Based on that, a model structure for the flame response to velocity and equivalence ratio

perturbations is suggested and the individual transfer functions are introduced.

2.1. Entropy and temperature fluctuations

A flame converts chemically stored enthalpy to sensible enthalpy h_s by means of a chemical reaction. The local change in specific sensible enthalpy imposed by a flame is given by the heat of reaction Δh_R. Therefore, locally at the flame front, the heat

$$\mathrm{d}q = \Delta h_R \tag{1}$$

is added to the fluid per unit mass. Upstream fluctuations of equivalence ratio and, hence, Δh_R will thus result in fluctuations of temperature downstream of the flame. Following Chu and Kovasznay[28] such temperature fluctuations are assigned to the entropy flow mode, which distinguishes them from isentropic fluctuations induced by a sound wave.[29] The linearised thermodynamic relation

$$\frac{s'}{c_p} = \frac{T'}{\bar{T}} \tag{2}$$

relates normalised temperature to entropy fluctuations for negligible contributions of pressure, where c_p signifies the specific capacity of heat at constant pressure.[11] Throughout the paper, mean quantities are denoted by an overbar$\bar{\cdot}$ while a primed quantity$'$ indicates a fluctuation around this mean. Following equation (2) temperature fluctuations are always assumed to be entropic within this paper. This is especially true for all presented CFD results which result from an incompressible formulation.

2.2. Generation of entropy fluctuations

Mass flux weighted integration of the total local heat release rate $\mathrm{d}\dot{Q} = \dot{m}\mathrm{d}q$ over the whole flame surface A_{fl} yields the integral heat release rate. Here, $\dot{m}$ denotes the local mass flux across the flame surface. As explained by Lieuwen,[30] within the linear regime and for negligible variations in upstream density, the integral heat release rate fluctuation is composed of three terms

$$\frac{\dot{Q}'}{\bar{\dot{Q}}} = \underbrace{\frac{\int_{\bar{A}_{\mathrm{fl}}} \Delta h_R' \mathrm{d}A}{\int_{\bar{A}_{\mathrm{fl}}} \Delta \bar{h}_R \mathrm{d}A}}_{\substack{\text{Local Heat Addition} \\ \rightarrow T' \neq 0}} + \underbrace{\frac{\int_{\bar{A}_{\mathrm{fl}}} s_f' \mathrm{d}A}{\int_{\bar{A}_{\mathrm{fl}}} \bar{s}_f \mathrm{d}A}}_{\substack{\text{Flame Consumption Rate} \\ \rightarrow T' \approx 0}} + \frac{A_{\mathrm{fl}}'}{\bar{A}_{\mathrm{fl}}} \tag{3}$$

where s_f denotes the flame speed. The first term accounts for fluctuations in the heat of reaction, the second for fluctuations in flame speed and the last for fluctuations of the flame surface area.

For the sake of clarifying the relation between heat release of a flame and the production of temperature inhomogeneities, an example is discussed: A flame burning at a steady state is considered, which is disturbed by a sudden increase in the inlet velocity. In this case, the flame speed and the heat of reaction stay approximately constant. It follows from equation (1) that the local specific heat added to the fluid does not change anywhere along the flame surface. Hence, no temperature inhomogeneities are generated. On the other hand, the increasing velocity has to lead to an increase in the total flame surface because this is the only possibility to consume the additionally provided unburned mixture. According to equation (3) this will result in a rise of the integral heat release rate. Consequently, the integral heat release changes, while the sensible enthalpy generated by the flame is not affected. This result was also retrieved by Strobio Chen et al.[24] who showed that velocity perturbations produce changes of sensible enthalpy that are only of first order in Mach number. Since flames are usually stabilised at regions of low flow speed, those contributions can often be neglected. According to equation (1) only changes in the heat of reaction affect the heat, which is locally added to the fluid per unit mass. Hence, only sufficiently strong changes in the heat of reaction lead to a significant generation of temperature inhomogeneities, as it occurs for equivalence ratio forcing.

Based on these considerations, the above-mentioned coupling of the generation of temperature fluctuations to the integral heat release does not seem appropriate. A physically correct coupling requires compensation for consumption rate fluctuations of the flame. This was implemented in several studies by introducing a moving flame front to the models,[24] i.e. respecting the fact that part of the heat release only affects the global flame consumption rate and, thus, does not influence the temperature of the burned gases, see equation (3). Although this method leads to adequate models, its practical applicability is limited. The main problem is to separate the different contributions to the overall heat release rate. Such a segregation might work for generic flame models, like the one proposed by Cho and Lieuwen,[31] but fails for real flames, where the individual contributions to the global heat release are hard to be accessed. As shown in section 3.3, there are indeed significant differences between the response of a flame to equivalence ratio in terms of heat release and temperature. Furthermore, a spatially integrated consideration of the production of temperature inhomogeneities neglects the so-called advective dispersion, which is a two-dimensional (2D)/three-dimensional (3D) phenomenon (see section 5.2).

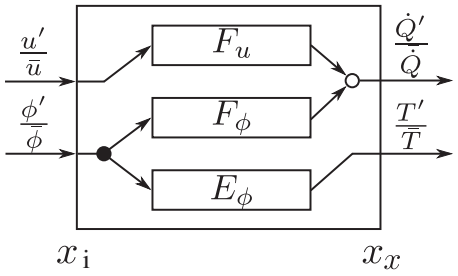

Figure 2. Schematic drawing of the flame response as a multiple-input multiple-output system containing the flame transfer function with respect to velocity F_u as well as the flame transfer function F_ϕ and the entropy transfer function E_ϕ, both with respect to the equivalence ratio. Inputs are velocity and equivalence ratio fluctuations at a reference position x_i, outputs variations in heat release and temperature at a source position x_x.

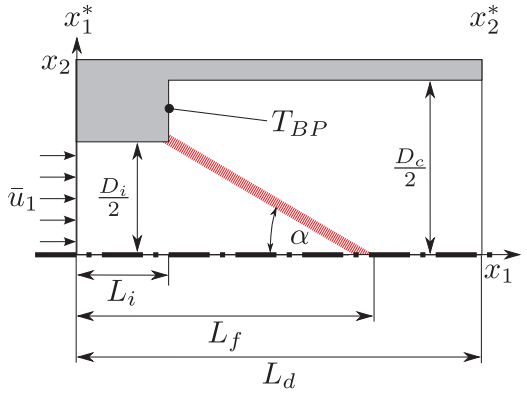

Figure 3. Sketch of a flame stabilised at a backward facing step.

2.3. Structure of flame models

In order to correctly account for the thermoacoustic effects of a technically premixed flame, the individual forms of sound generation, related to the presence of the flame, have to be modelled separately. This leads to a representation of a technically premixed flame as a so-called multiple-input multiple-output (MIMO) system, as illustrated in Figure 2.[32] The two inputs (u' and ϕ') have to be related to the two outputs (Q' and T'). The transfer functions required for this are described in the following.

We distinguish between two classes of transfer functions, depending on whether they contribute to either direct or indirect sound production: The first class comprises the well-known flame transfer functions (FTFs), which relate upstream flow perturbations to fluctuations in heat release rate. In particular, the transfer functions F_u and F_ϕ describe the response to fluctuations in axial velocity u_i' and equivalence ratio ϕ_i' at a reference position x_i, respectively. The second class comprises the indirect transfer functions, which within the present analysis consist only of the entropy transfer function E_ϕ. This transfer function relates equivalence ratio perturbations at a position x_i to the resulting variations in the exhaust gas temperature at x_x. In general, the positions x_i and x_x have to be chosen individually for each input and output channel. To simplify the presentation of ideas, we chose not to discriminate between the reference positions for the individual channels.

3. Numerical analysis

In the following, the flame response to equivalence ratio forcing is analysed numerically using adiabatic test case setups. Two laminar premixed flames with different Péclet numbers Pe and, thus, a different relative importance of diffusion and advection, are analysed. Firstly, steady state fields are computed. These data are required for the models proposed in sections 5.2 and 5.3. Secondly, transfer functions for entropy E_ϕ and heat release F_ϕ are identified from transient CFD simulations. The former are used in section 6 to validate the proposed models.

Table 1. Parameters for both investigated validation cases.

	Pe = 90	Pe = 450
$\bar{u}_i$	1.0 $\frac{m}{s}$	1.0 $\frac{m}{s}$
D_i	2 mm	10 mm
D_c	5 mm	25 mm
L_i	1 mm	10 mm
L_d	8 mm	40 mm
L_{CFD}	10 mm	60 mm
T_{BP}	Adiabatic	Adiabatic

3.1. Test case setup

Two setups with the respective Péclet numbers of Pe = 90 and Pe = 450 are investigated. Both lean methane-air flames are operated at a mean equivalence ratio of $\bar{\phi} = 0.8$. As it will be shown in section 4, the thermodynamic relations of interest are fairly linear here. Since complex phenomena such as turbulence or unsteady coherent structures are excluded, both setups serve as clean and well defined validation cases for the proposed models.

The geometrical details are sketched in Figure 3 and the corresponding numerical values are provided in Table 1 for both cases. In each of them, an inclined flame (fat line) with a flame angle α is stabilised at a backward facing step connecting a feed channel (diameter D_i and length L_i) to a combustion chamber (diameter D_c). At the inlet of the domain, which corresponds

to the reference position x_i, a constant velocity profile of $\bar{u}_i$ is imposed. The axial distance from the inlet to the outlet reference position x_x is denoted as L_d, the one to the tip of the flame as L_f. The length of the computational domain L_{CFD} is chosen to be larger than L_d. Based on these quantities, Péclet numbers are defined by $\mathrm{Pe} = \bar{u}_i D_i / D_{\mathrm{CH4,\,air}}$ using the diffusivity of methane in air $D_{\mathrm{CH4,\,air}}$ at 300 K. All boundaries are adiabatic, except the walls of the feed channel for the $\mathrm{Pe} = 450$ case. Here, a fixed temperature of 300 K is imposed, which is necessary to suppress flame flashback into the feed channel. Since wall and fluid temperature are identical here, those walls can approximately also be considered to be adiabatic. Both setups have an identical confinement ratio of $D_i/D_c = 0.4$.

3.2. Steady state CFD

Incompressible 2D simulations are performed using the open source software OpenFOAM.[33] Chemical reactions are respected by adopting the reduced chemical kinetic two-step mechanism (2S-CM2) proposed by Bibrzycki et al.[34] Schmidt numbers for all six considered species are set according to Duchaine et al.[35] This solver setup has already been used by Jaensch et al.[36] to study nonlinear thermoacoustic oscillations and successfully cross-validated the results against AVBP (see http://cerfacs.fr/en/computational-fluid-dynamics-softwares). Also, the transfer functions and mean fields for the $\mathrm{Pe} = 90$ case agree well with the recently published results of Strobio Chen et al.[25]

For the case with $\mathrm{Pe} = 90$, a uniform structured rectangular grid with a cell density of 40cells/mm^2 is used. The flame region of the $\mathrm{Pe} = 450$ setup is resolved by the same cell density. However, downstream of that region a slight increase of the axial cell width towards the boundaries is adopted. At the inlet boundary, an inflow of 300K with a rectangular axial velocity profile and a zero gradient pressure condition are imposed. At the outlet, the pressure is fixed to a constant value and the velocity to a zero gradient.

Steady state solutions for both Péclet numbers are presented in Figure 4. Here, the colour depicts the temperature field. The laminar flow is indicated by streamlines (white, continuous lines) and an approximate position of the flame front is provided by an iso-temperature line (- - -). Additionally, so-called iso-τ lines are shown (·-o-·). These connect points of the same advective time delay with respect to the inlet. For each configuration, six iso-τ lines are plotted, which are uniformly distributed between zero and the time delay measured at the fastest streamline at the outlet reference position. Strong spatial gradients of these lines can be observed, resulting on the one hand from wall friction and the acceleration at the inclined flame front on the other. Such gradients lead to a temporal dispersion of the mass flux averaged temperature fluctuations measured at a reference position. Hence, this effect is referred to as advective dispersion.[37,38]

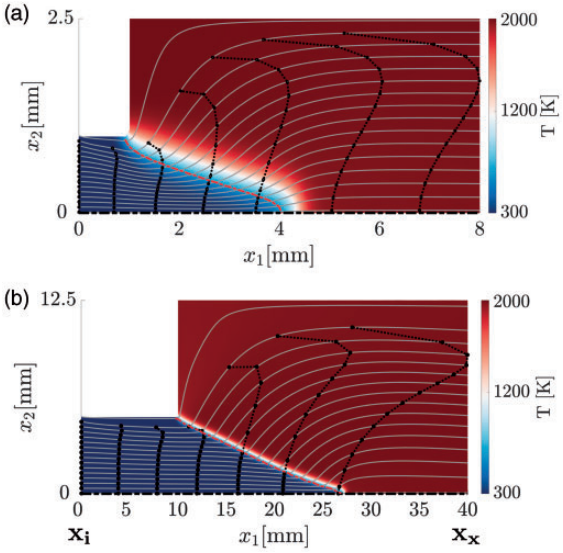

Figure 4. Steady state computational fluid dynamics solution of the $\mathrm{Pe} = 90$ (4(a)) and $\mathrm{Pe} = 450$ (4(b)) cases. Colour represents the temperature field. Streamlines (——), an estimate for the flame front (- - -) and six iso-τ lines (·-o-·) are also shown.

3.3. CFD/SI

We now employ unsteady CFD simulations in order to determine the ETF for both setups. A broad band[39] temporal variation of the equivalence ratio at the inlet of the CFD domain x_i is imposed $\phi(t) = \bar{\phi} + \phi'(t)$ (input time series) and the mass flux averaged temperature fluctuation at the reference plane x_x (output I) as well as the integrated heat release inside the flow domain (output II) are recorded. The equivalence ratio forcing is realised by varying the mass fraction of CH_4 at the inlet according to

$$y_{\mathrm{CH_4}}(t) = \frac{M_{\mathrm{CH_4}}}{M_{\mathrm{CH_4}} + \frac{2}{\phi(t)}\left(M_{\mathrm{O_2}} + 3.7619 M_{\mathrm{N_2}}\right)}, \qquad (4)$$

where $M_{\mathrm{CH_4}}$, $M_{\mathrm{O_2}}$ and $M_{\mathrm{N_2}}$ are the molar masses of methane, oxygen and nitrogen, respectively. Air with 21% oxygen and 79% nitrogen by volume is assumed. The change in $y_{\mathrm{CH_4}}$ is compensated by the mass fraction of nitrogen $y_{\mathrm{N_2}}(t) = 1 - y_{\mathrm{O_2}} - y_{\mathrm{CH_4}}(t)$ with the mass fraction of oxygen being fixed to $y_{\mathrm{O_2}} = 0.222523$. In this way, only negligible fluctuations in velocity result from the modulation of equivalence ratio.[25]

SI techniques are utilised in order to estimate the desired ETF from the input/output time series of the transient CFD data. The imposed broad band signal has a cut-off frequency well above the expected cut-off of the expected transfer function. A so-called finite impulse response (FIR) model is fitted to the broad band input/output data. It has been shown that this kind of model is capable of capturing the system behaviour with quantitative accuracy.[25,27,40] The ETF is computed from relating output I, the FTF F_ϕ from relating output II to the input time series. Both transfer functions can be estimated independently. Compared to the evaluation of the frequency responses (FRs) for a certain number of discrete frequencies by repeated simulations with harmonic forcing, the CFD/SI method with broad-band forcing has the advantage that it requires only a single simulation. The total simulation time and hence the total computational effort are significantly reduced.[27] Also note that CFD/SI yields a proper FTF, which may be evaluated at complex-valued frequencies, while harmonic forcing yields only the FR. This has significant advantages for stability analysis, which requires an evaluation of the FTF at complex-valued frequencies. Furthermore, CFD/SI directly estimates the impulse response (IR), which provides additional insight into the physical processes involved.

The time series data are split into a training (80%) and a test data set (20%). The training data are used for fitting the FIR model, the latter to assess the quality of this fit. The resulting transfer functions can be visualised in the time domain as the IR, which is plotted in Figure 5 (left) for the ETF, and in Figure 6 (left) for the FTF with respect to ϕ. In each of these figures, the corresponding frequency response function (FRF) is displayed in terms of magnitude and phase on the right. Note that the FRF is only evaluated up to a frequency where the gain becomes close to zero. Comparing the predictions of the identified models with the test data set, good agreement is achieved (not shown).

Impulse and FRs are plotted versus non-dimensional parameters, which are denoted by a star .* superscript. For the ETF, a non-dimensional advective timescale $t_a^* = t/\tau_\mathrm{a}$ is introduced with a reference time lag of $\tau_\mathrm{a} = L_d/\bar{u}_i$. That way, a non-dimensional time delay of unity corresponds to the time it takes for a fluid particle to travel with the bulk flow velocity measured at the inlet along a straight axial line between the two reference positions x_i and x_x. For the transfer function F_ϕ, the characteristic time of restoration, defined by Blumenthal et al.,[41] $\tau_\mathrm{f} = D_i/(2\cos(\alpha)\sin(\alpha)\bar{u}_i)$ is applied as reference, which yields a non-dimensional flame time scale t_f^*. A non-dimensional time delay of unity corresponds to the time it takes for a flame wrinkle to travel from the flame base to the tip. The corresponding Strouhal numbers f_a^* and f_f^* are computed by normalising the frequency with the inverse of the reference time lag, i.e. $f^* = f\tau_\mathrm{ref}$.

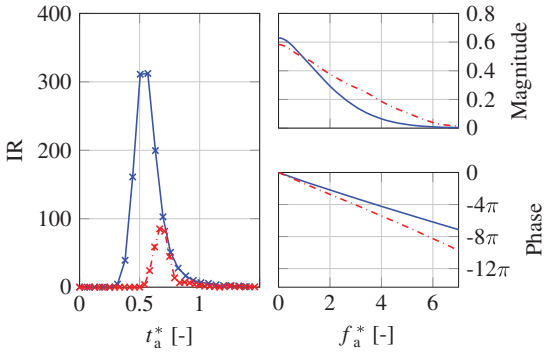

Figure 5. Entropy response E_ϕ plotted in the time (left) and the frequency domain (right). Pe = 90 (——); Pe = 450 (-·-·-).

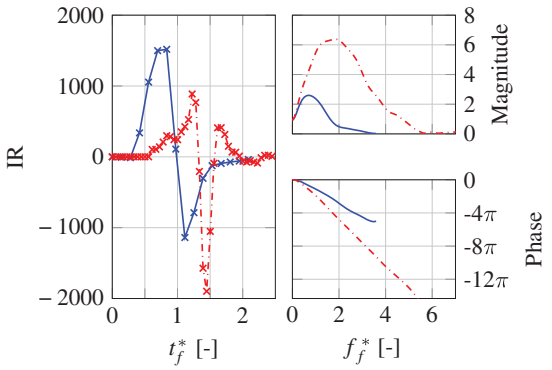

Figure 6. Heat release response F_ϕ plotted in the time (left) and the frequency domain (right). Pe = 90 (——); Pe = 450 (-·-·-).

Interpreting the resulting IRs of the ETF, it has to be considered that the time axis of the Pe = 90 case is non-dimensionalised by a smaller advective time scale than for the Pe = 450 case. Hence, the IR at high Péclet-number seems to be less dispersed in time than the low Péclet case, while it is the other way round when plotted in dimensional form.

The effect of advective dispersion has previously been modelled by evaluating the probability density function (PDF) of the residence time of a mass-less particle advecting from the inlet to a reference position. The retrieved PDFs can be interpreted as the IR of the transfer function governing the transport processes. For example, Polifke et al.[37] analysed the transport of mass-less particles from a fuel injector to a swirl stabilised flame front. Morgans et al.[38] investigated the transport of temperature inhomogeneities inside a fully developed, turbulent channel flow. It was found

by both studies that the determined PDF essentially follows a Gaussian distribution of a certain width around a mean time delay. While these two studies focused either on the transport processes of equivalence ratio/temperature fluctuations inside the unburned/burned flow domain, the present study analyses both effects combined. Three mechanisms are captured: the transport of equivalence ratio fluctuations to the flame, its conversion to temperature inhomogeneities and the transport of the latter to a reference position.

Evaluating the ETF for the two test setups, a Gaussian like IR is retrieved (Figure 5). The corresponding FR shows a low-pass filter behaviour, without any excess of gain or local maxima in the magnitude. The FTF for equivalence ratio fluctuations shows a completely different behaviour (see Figure 6). Here, a very pronounced excess of gain can be noticed, which is not present at all in the ETF. Hence, as stated in the introduction, the ETF cannot easily be coupled to the integral heat release. The (linear) dynamics of the heat release is determined by many effects (surface area, flame speed, heat of reaction)[31,42] and is, thus, richer than the dynamics of the ETF, which is essentially governed by the mean flame shape and convective transport. Therefore, the response of technically premixed flames in terms of heat release and temperature fluctuations should generally be modelled as a MIMO system, see Figure 2.

4. Fast-reaction-zone (FRZ) model

In this section, we focus on the transformation of equivalence ratio to temperature fluctuations at the flame. Transport processes are neglected and the flame is viewed as an infinitely thin discontinuity, separating the burned from the unburned mixture. This FRZ model instantaneously translates upstream fluctuations in equivalence ratio to downstream variations in temperature, as it is depicted in Figure 7. Here, an index 'u' refers to a position upstream of the flame inside the unburned, an index 'b' to a position downstream inside the burned mixture. For ETF predictions, this model needs to be combined with a model for the convective transport processes before and behind the flame. Three of such models are proposed in section 5.

We assume that the temperature at the unburned side of the flame is constant. The FRZ model is valid as long as, locally, chemical time scales $\tau_{\text{chem}} \approx D_{\text{CH}_4,\text{air}}/s_f^2$ are much shorter than the ones of the excitation signal $\phi_u'(t)$. Here, $D_{\text{CH}_4,\text{air}}$ is the diffusivity of methane in air and s_f the laminar flame speed. For the investigated setups, this holds for excitation frequencies up to approximately 3000 Hz, which is far beyond the highest identified cut-off frequency of the ETF ($\approx$ 700 Hz). Thus, for sufficiently low frequencies

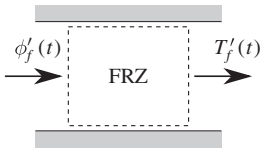

Figure 7. Representation of the flame as a fast-reaction-zone, relating downstream fluctuations in temperature of the burned (index 'b') to upstream equivalence ratio perturbations of the unburned mixture ('u').

and small amplitudes, the transfer function relating the input to the output signal reduces to a static gain ϑ_{FRZ}

$$\frac{T_b'}{\bar{T}_b} = \vartheta_{\text{FRZ}}(\bar{\phi}_u)\frac{\phi_u'}{\bar{\phi}_u}. \tag{5}$$

Note that this static gain depends on the mean equivalence ratio of the reactants.

In the following, this equivalence ratio dependent factor is analysed for lean methane-air mixtures, first by employing a numerical model including detailed chemistry and then by analytic considerations.

4.1. Numerical model

In order to numerically evaluate the behaviour of ϑ_{FRZ}, the software Cantera[43] is employed. For a given mixture, it numerically computes the chemical equilibrium which here corresponds to the burned state of the mixture under adiabatic and isobaric conditions. The temperature reached is hence the adiabatic flame temperature. Employing the detailed chemical reaction scheme GRI-Mech 3.0,[44] the adiabatic flame temperature is computed for a range of equivalence ratios (see Figure 18 (top) in Appendix 1). We now assume T_b equals the adiabatic flame temperature T_{ad}. Equation (5) is then applied to evaluate the corresponding static gain factor by numerical differentiation using a central difference scheme

$$\vartheta_{\text{FRZ}}(\bar{\phi}_u) = \frac{\bar{\phi}_u}{\bar{T}_b}\,\frac{T_b(\bar{\phi}_u + \Delta\phi) - T_b(\bar{\phi}_u - \Delta\phi)}{2\Delta\phi}. \tag{6}$$

Applying a spacing of $\Delta\phi = 0.01$, $\vartheta_{\text{FRZ}}(\bar{\phi}_u)$ is evaluated for $0.6 \le \bar{\phi}_u \le 1.2$. The resulting curve is plotted in Figure 8 (——). Independence of the solution from the spacing $\Delta\phi$ has been checked. ϑ_{FRZ} is approximately constant for $\bar{\phi}_u \lesssim 0.8$ and then drops to zero when approaching stoichiometric conditions. This drop can be explained by incomplete combustion at high temperatures. As stoichiometric conditions are reached, the temperature of the combustion products reaches a maximum. At such a high temperature, however, the chemical equilibrium of the mixture is at a

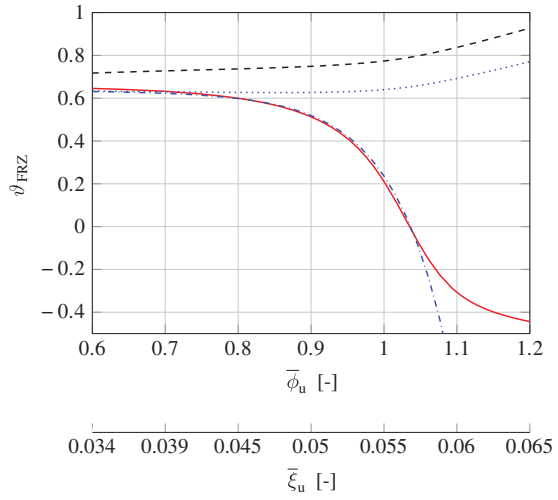

Figure 8. Static gain ϑ_{FRZ} plotted over the mean equivalence ratio $\bar{\phi}_u$ as well as the mean mixture fraction $\bar{\xi}_u$: Data from numerical simulation using detailed chemistry (——); proposed model from equation (15) (-·-·-); proposed model neglecting the term respecting incomplete combustion C_{inc} from equation (14) (-·-·-); proposed model neglecting the term C_{inc} and omitting influence of fluctuations in c_p (- - -).

point where not all reactants have been transformed completely to products. Thus, not all of the reaction enthalpy stored in the chemical compounds is released. Consequently, this leads to a lower temperature of the burned mixture than it would be expected by a linear relation between the chemically available enthalpy and T_b. It can hence be deduced that the importance of entropy noise also decreases for $\bar{\phi}_u \to 1$. For rich mixtures the static gain becomes negative, since an increase in equivalence ratio leads to incomplete combustion and to an increase of the specific heat capacity of the burned gases due to unburned reactants. Hence, the temperature of the burned mixture decreases and ϕ'_u and T'_b are in antiphase.

4.2. Analytical model

We now develop an analytical model for ϑ_{FRZ}. For that purpose, we firstly analyse the relevant physical processes before we introduce the modelling concepts. Three points are important:

1. Assuming complete combustion, i.e. all of the carbon and hydrogen of the fuel is converted to CO_2 and H_2O respectively, the difference of the enthalpies of formation of the reactants and products is transformed to sensible enthalpy. A fluctuation in equivalence ratio will change the mass fraction of fuel and hence the sensible enthalpy of the burned mixture.
2. Fluctuations of equivalence ratio and, hence, sensible enthalpy also lead to fluctuations in the specific heat capacity c_p, which significantly influences the temperature fluctuations of the combustion products.
3. Approaching stoichiometric conditions, the combustion process is not complete anymore. This results in a drop of the amplitude of the temperature fluctuations.

We start with point one. If the reactants are at standard-state reference conditions ($T_{ref} = 298.15\text{K}$ and $p_{ref} = 1\text{bar}$), the change of sensible enthalpy due to chemical reactions can be computed from the lower heating value (LHV) H_l and the mass fraction of methane y_{CH4} by $\Delta h_R = y_{CH_4} H_l$. The quantity Δh_R is also called the enthalpy of combustion or the heat of reaction. By introducing the definition of equivalence ratio

$$\phi = \frac{y_{CH4}/y_{air}}{1/l_{st}} \tag{7}$$

with the mass fraction of air y_{air} and the stoichiometric air-to-fuel ratio $l_{st} = (y_{air}/y_{CH4})_{st}$, this results in an expression

$$\Delta h_R = \frac{H_l}{1 + \frac{l_{st}}{\phi}}. \tag{8}$$

For methane with $H_l \approx 50.01\,\frac{\text{MJ}}{\text{kg}}$ and $l_{st} \approx 17.13$, this leads to the formula provided by Abu-Off and Cant[45] and Lieuwen.[30] Linearising this relation yields

$$\frac{\Delta h'_R}{\overline{\Delta h_R}} = \frac{1}{1 + \frac{\bar{\phi}_u}{l_{st}}} \frac{\phi'_u}{\bar{\phi}_u}. \tag{9}$$

Since $\bar{\phi}_u \ll l_{st}$ holds, normalised fluctuations in heat of reaction approximately correspond to normalised equivalence ratio fluctuations.

We now focus on the second point. For small fluctuations of equivalence ratio, the change in the heat of reaction can be expanded to

$$\Delta h'_R = \left[\frac{\partial}{\partial \phi} \int_{\tilde{T}_u}^{T_b(\phi)} c_p(\tilde{T}, \phi) \mathrm{d}\tilde{T} \right]_{\bar{\phi}_u} \phi'_u + \mathcal{O}(\phi'_u \phi'_u) \tag{10}$$

where the specific heat capacity c_p is a function of temperature and equivalence ratio. Note that the upper integration limit also depends on the equivalence ratio. Application of the Leibniz integral rule and neglecting $\mathcal{O}(\phi'_u \phi'_u)$ terms results in

$$\Delta h'_R = \left[\frac{\partial T_b(\phi)}{\partial \phi} c_p(T_b(\phi), \phi) + \int_{\tilde{T}_u}^{T_b(\phi)} \frac{\partial c_p(\tilde{T}, \phi)}{\partial \phi} \mathrm{d}\tilde{T} \right]_{\bar{\phi}_u} \phi'_u. \tag{11}$$

Inserting the relation $T_b' = (\partial/\partial\phi)T_b(\phi)\big|_{\bar{\phi}_u}\phi_u'$, defining $c_{p,b} := c_p\left(\bar{T}_b, \bar{\phi}_u\right)$ and neglecting $\mathcal{O}\left(\phi_u' c_p'\right)$ terms leads to

$$\Delta h_R' = T_b' c_{p,b} + \phi_u' \int_{\bar{T}_u}^{\bar{T}_b} \left.\frac{\partial c_p\left(\tilde{T},\phi\right)}{\partial\phi}\right|_{\bar{\phi}_u} \mathrm{d}\tilde{T}. \tag{12}$$

A change in heat of reaction due to ϕ_u', therefore, goes along with a temperature and a specific heat capacity variation. If c_p increases with $\bar{\phi}_u$, the temperature variation caused by an increased Δh_R is smaller than if c_p were constant.

We write the integral of the second term of equation (12) as a product $I_{c_p}\left(\bar{T}_b - \bar{T}_u\right)$ and end up with a relation between fluctuations in temperature, specific heat capacity and heat of reaction

$$\frac{\Delta h_R'}{\overline{\Delta h}_R} = \frac{c_{p,b}\bar{T}_b}{\overline{\Delta h}_R}\left[\frac{T_b'}{\bar{T}_b} + \frac{\bar{\phi}_u I_{c_p}}{c_{p,b}}\left(1 - \frac{\bar{T}_u}{\bar{T}_b}\right)\frac{\phi_u'}{\bar{\phi}_u}\right]. \tag{13}$$

For lean methane-air mixtures, I_{c_p} is approximately a constant and can be estimated using the trapezoidal rule (see Appendix 1).

By combining equations (9) and (13) and using relation equation (8) to rewrite $\overline{\Delta h}_R$, we obtain a relation between equivalence ratio and temperature fluctuations

$$\vartheta_{\mathrm{FRZ}}\left(\bar{\phi}_u\right) = \frac{H_l}{c_{p,b}\bar{T}_b}\frac{\bar{\phi}_u l_{\mathrm{st}}}{\left(\bar{\phi}_u + l_{\mathrm{st}}\right)^2} - \frac{\bar{\phi}_u I_{c_p}}{c_{p,b}}\left(1 - \frac{\bar{T}_u}{\bar{T}_b}\right). \tag{14}$$

Plotting this factor over mean equivalence ratio results in the dotted line (·····) shown in Figure 8. Up to $\bar{\phi}_u \approx 0.8$ it agrees very well with the numerical results from the Cantera simulations. When approaching stoichiometric conditions, incomplete combustion becomes more and more relevant which violates the assumptions of the analytical model. As a result of this, it predicts too high values for the static gain.

If we neglect variations of the specific heat capacity, i.e. $I_{c_p} = 0$, we end up with a prediction of the static gain as it is plotted with the dashed line (- - -). Here, only fluctuations of $T_b(\phi)$ (equation (10)) and the heat of reaction (equation (9)) are respected. For $\bar{\phi}_f \lesssim 0.8$ it deviates from the reference line (——) by about 15 %. Therefore, variations in c_p due to changes in the mixture composition significantly influence the flame response in terms of downstream temperature.

The drop of the static gain due to incomplete combustion, see aforementioned point three, can be accounted for by introducing an empirical term $C_{\mathrm{inc}}(\bar{\phi})$. It is obtained by minimising the error of equation (14) for $0.75 < \bar{\phi}_u < 1.05$ with respect to the numerical simulation data. Details on the derivation are provided in Appendix 1.

Putting all three effects together, we end up with a model

$$\vartheta_{\mathrm{FRZ}}\left(\bar{\phi}_u\right) = \underbrace{\frac{H_l}{c_{p,b}\bar{T}_b}\frac{\bar{\phi}_u l_{\mathrm{st}}}{\left(\bar{\phi}_u + l_{\mathrm{st}}\right)^2}}_{\text{change in temperature/ heat of reaction}} - \underbrace{\frac{\bar{\phi}_u I_{c_p}}{c_{p,b}}\left(1 - \frac{\bar{T}_u}{\bar{T}_b}\right)}_{\text{change in specific heat}} - \underbrace{C_{\mathrm{inc}}(\bar{\phi})}_{\text{incomplete combustion}}. \tag{15}$$

Its predictions are plotted in Figure 8 (-·-·-). They match the reference line very well for all considered lean mean equivalence ratios.

5. Transport model

So far, a model for the combustion process has been developed (transformation $\phi_u' \rightarrow T_b'$). In the following, the transport processes before and after the flame are focused on. They are dominated by convection, which is defined as the superposition of advection and diffusion.

In technically relevant combustors, also the mixing of cold and hot air or fuel streams up- and downstream of the flame is important. Such mixing problems are of particular interest for diffusion flames. Here, a quantity called mixture fraction ξ is used to model the mixing (see e.g. Bilger[46]). It is defined in such a way that it yields unity inside the fuel stream (no air) and becomes zero in the air stream (no fuel) and can, hence, be denoted as the elemental mass fraction that emanates from the pure fuel stream

$$\xi = \frac{Z_{\mathrm{C}}}{\mu_{\mathrm{C,CH4}}} = \frac{1}{1 + l_{\mathrm{st}}/\phi} \tag{16}$$

with the element mass fraction of carbon Z_{C}. The latter can be computed by $Z_{\mathrm{C}} = \sum_{k=1}^{N} \mu_{\mathrm{C},k} y_k$ where the coefficients $\mu_{\mathrm{C},k}$ denote the mass fraction of carbon in the species k. This expression has to be evaluated using all N species of the burned/ unburned mixture. The mass fraction of carbon in methane can be specified as $\mu_{\mathrm{C,CH4}} \approx 0.749$. Since the amount of each element stays constant during the chemical reaction, this quantity is conserved during the combustion process.

Applying the concept of mixture fraction to the present, technically premixed flames, allows us to decouple the modelling of the combustion process from the

transport. This is a consequence of the fact that ξ is a conserved quantity and related to both the chemically stored enthalpy h_{chem} (unburned mixture) and the sensible enthalpy h_s (burned mixture). For adiabatic conditions and a Lewis number of unity, the knowledge of ξ hence allows us to infer the temperature of the combustion products. For small fluctuations of mixture fractions, a linear relation

$$\frac{\phi'}{\bar{\phi}} = \frac{1}{1-\bar{\xi}}\frac{\xi'}{\bar{\xi}} \tag{17}$$

connects normalised mixture fraction and equivalence ratio fluctuations. This can be used to directly relate fluctuations in mixture fraction to temperature fluctuations using equation (5). For that purpose, the abscissa in Figure 8 provides both mean mixture fraction and equivalence ratio.

In the following, first the basic modelling concept is introduced by a simple analytical 1D example: A solution for a 1D convection problem is provided and discussed, and the separation of the combustion and the transport processes for modelling purposes is explained. Based on this, two modelling strategies for the ETF are presented, which extend the ideas to higher dimensional cases: a so-called N1D model which consists of N 1D models connected in parallel and a state space (SS) model.

5.1. 1D model

We now analyse the generation of downstream temperature fluctuations T' at a reference position x_x by a ducted flame, resulting from upstream equivalence ratio fluctuations ϕ', as sketched in Figure 9. A heat release zone is placed inside a duct of a length L_{D} at an axial distance of L_{F} from the inlet. The fluid enters the domain at $x = x_i$ with a velocity u_i and leaves it at $x = x_x$ with a flow speed of u_x. An equivalence ratio forcing ϕ'_i is imposed at the inlet, which leads to temperature fluctuations T'_x at the outlet.

As already mentioned in section 4, the variable connecting equivalence ratio and temperature fluctuations

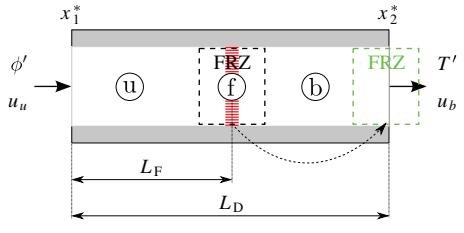

Figure 9. Sketch of a flame in a duct. The flame is modelled by the Fast reaction zone model.

is enthalpy. Its dynamics are described by the energy equation. For laminar adiabatic methane-air flames and a Lewis number of unity, this equation can be simplified to an advection-diffusion (AD) equation, as shown in Appendix 2

$$\rho\frac{\partial h}{\partial t} + \rho u\frac{\partial h}{\partial x_1} = \frac{\partial}{\partial x_1}\left(\rho D_f \frac{\partial h}{\partial x_1}\right). \tag{18}$$

Here, D_f denotes the diffusivity (molecular or heat), ρ the density and u the flow velocity. This convective transport equation comprises transport by advection (velocity field) and diffusion. For incompressible conditions, it is decoupled from the momentum equation and hence can be solved after a steady solution of the momentum and mass conservation is found. Combining equations (8) and (16) yields a linear mapping between fluctuations in enthalpy and mixture fraction $h' = \xi' H_l$. Inserting this relation into equation (18) results in a transport equation for the normalised mixture fraction fluctuation $\Xi = \xi'/\bar{\xi}$

$$\rho\frac{\partial \Xi}{\partial t} + \rho u\frac{\partial \Xi}{\partial x_1} = \frac{\partial}{\partial x_1}\left(\rho D_f \frac{\partial \Xi}{\partial x_1}\right) \tag{19}$$

which is valid everywhere in the flow domain. In the unburned part, it characterises the transport of chemical, whereas in the burned part that of sensible enthalpy. Using the static gain factor ϑ_{FRZ} and combining equations (5) and (17), the local temperature of the burned fluid is computed from Ξ by

$$\frac{T'}{\bar{T}} = \frac{\vartheta_{\mathrm{FRZ}}}{1-\bar{\xi}}\,\Xi. \tag{20}$$

The ETF of the 1D duct can be represented by a cascade of linear transfer functions, as shown in Figure 10(a). Physically, equivalence ratio fluctuations are convected from the inlet to the flame, where they are transformed to temperature fluctuations by the combustion process, which are subsequently convected to the domain outlet. By applying equation (19) this problem is transformed to a different one: At the inlet we need to transform the equivalence ratio forcing to the corresponding normalised mixture fraction fluctuation Ξ. This quantity can then be transported until the outlet is reached, using the corresponding flow velocities and diffusion coefficients. At the outlet, Ξ is mapped to a temperature fluctuation. The associated connection of transfer elements is shown in Figure 10(b). Hence, the proposed modelling strategy changes the order of the transfer functions. Due to the linearity of the problem, this is a valid operation. It can be depicted as moving the FRZ model to the end of the duct in Figure 9. The problem is split into two

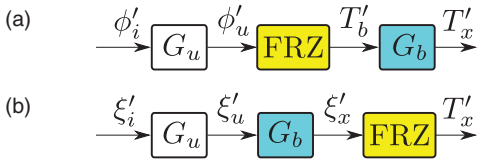

Figure 10. Cascade of transfer functions of the entropy transfer function connecting T_x' and ϕ_i'. Convective transport processes are modelled by the transfer functions G_u and G_b. Models for them are provided in section 5. The combustion process is modelled by the Fast-reaction-zone model described in section 4. (a) Representation of the physics: A fluctuation of equivalence ratio ϕ_i' is transported from the inlet x_i to the flame front (G_u), where it generates a temperature modulation T_b'(FRZ), which is then transported in the burned part to the downstream reference position x_x (G_b). (b) Modelling strategy: a fluctuation of mixture fraction ξ_i' is transported from the inlet x_i to the outlet x_x (G_u and G_b), where ξ_x' is mapped to a temperature fluctuation T_x' (FRZ).

simpler problems: (1) The transport of normalised mixture fraction fluctuations Ξ and (2) the transformation of Ξ to temperature fluctuations T' (combustion). This simplifies the treatment significantly, especially in the 2D case as it will be shown in the following sections.

We now analytically solve the 1D transport problem given by equation (19) for a constant flow velocity. Its IR is written as

$$h(t) = D(x_1, t) * \delta\left(t - \frac{x_1}{u}\right), \tag{21}$$

where $*$ is the convolution operator in x_1 and $\tau_i = x_1/u$ is the advective time delay. The expression D denotes Green's function computed as the solution of

$$\frac{\partial \Xi(x_1,t)}{\partial t} = D_f \frac{\partial^2 \Xi(x_1,t)}{\partial x_1^2} \tag{22}$$

$$\Xi(x_1, 0) = \delta(x_1) \tag{23}$$

$$\lim_{x_1 \to \pm\infty} \Xi(x_1, t) = 0 \tag{24}$$

which is a pure diffusion problem including free boundary conditions and an initial disturbance by a Dirac impulse. Hence, the solution to this is the IR

$$D(x_1, t) = \frac{\Theta(t)}{\sqrt{4\pi D_f t}} \exp\left[-\frac{x_1^2}{4D_f t}\right] \tag{25}$$

with the Heaviside step function $\Theta(t)$. Following equation (21) the transport problem can be interpreted as an impulse travelling with flow speed along a streamline while being diffused according to equation (25).

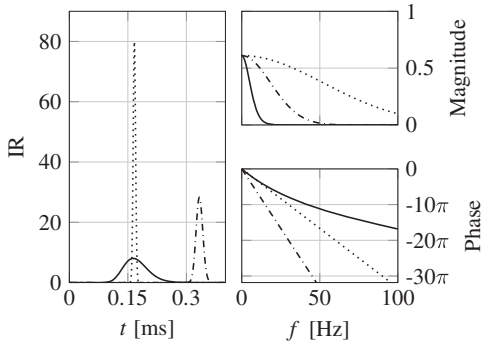

Figure 11. Entropy response of a one-dimensional duct: $u = 0.6$ m/s and $D_f = 1 \cdot 10^{-3}$ m^2/s (——); $u = 0.6$ m/s and $D_f = 1 \cdot 10^{-5}$ m^2/s (·····); $u = 0.3$ m/s and $D_f = 1 \cdot 10^{-5}$ m^2/s (-·-·-).

Evaluating the convolution of equation (21) using equation (25) results in an expression

$$\begin{aligned} h(t) &= uD(x_1 - ut, t) \\ &= \frac{u\Theta(t)}{\sqrt{4\pi D_f t}} \exp\left(-\frac{(x_1 - ut)^2}{4D_f t}\right). \end{aligned} \tag{26}$$

For a given reference position x_1 this defines the IR of the convection problem in time. A mapping to frequency domain yields

$$F_i(\omega) = \frac{u}{\sqrt{4D_f i\omega + u^2}} \exp\left[\frac{x_1}{2D_f}\left(u - \sqrt{4D_f i\omega + u^2}\right)\right]. \tag{27}$$

Applying equation (20) at the outlet results in the ETF of this 1D problem. The properties of this solution are illustrated by an example given below. We assume a configuration as sketched in Figure 9 with a duct length of $L_D = 10$ cm and a mean equivalence ratio of $\bar{\phi} = 0.8$. Two different flow velocities and two diffusion coefficients are considered (see Figure 11), which are constant and the same for the burned and the unburned region. Therefore, the position of the flame is irrelevant. Note that this is usually not the case, since the higher temperature of the burned fluid usually enhances diffusivity and also leads to an acceleration of the flow. Thus, for realistic conditions, two ducts, one for the unburned (G_u) and one for the burned (G_b) region, have to be connected in a row (see Figure 10(b)).

The resulting IRs of the ETF according to equation (26) are plotted in Figure 11 on the left side for three configurations. The corresponding FRs according to equation (27) are depicted on the right (in terms of gain and phase). The mapping proposed by equation (20) is applied to compute temperatures at the outlet.

In the time domain, an enhanced diffusivity leads to a more spread out distribution of the IR. This translates to a lower cut-off frequency in the frequency domain. Diffusion, thus, dampens high frequency oscillations. Moreover, the slope of the phase is decreased. This means the effective time delay between the input signal and the output signal is reduced. This is a result of the increased transport velocity, which is the sum of advection (flow speed) and diffusion. A change in flow velocity essentially results in a shifted peak in the IR. This shift only affects the phase of the corresponding transfer function. Since the flow velocity also determines the time interval during which diffusive processes can act on an impulse, a change in velocity also affects the temporal spread of the IR. This, in turn, affects the magnitude of the transfer function.

5.2. N1D model

The modelling concepts presented so far are now extended to also consider 2D/3D geometries. An example setup is shown in Figure 12. The colour signifies the absolute flow velocity from the steady state CFD simulation, the flame front is indicated by a dashed line and the flow topology is illustrated by streamlines. We now track a fluid particle on its way from the inlet to the outlet along the highlighted streamline (——). Just like in the 1D duct case depicted in Figure 9, it is first transported by the unburned flow, passing the flame and then carried to the outlet by the burned fluid. Therefore, neglecting lateral ('cross-streamline') transport processes, the ETF of each streamline can be approximated by a 1D duct. The advection velocity and diffusion coefficients are extracted from the CFD data. This is done by projecting the flow velocity in tangential direction on each streamline. Local diffusion coefficients are evaluated from the temperature field by using the Chapman–Enskog theory as proposed by Poling et al.[47] For 300K, this results in a diffusivity of $D_{\mathrm{CH_4,air}} \approx 0.225\mathrm{cm}^2/\mathrm{s}$. Since we assume a Lewis number of unity, the thermal diffusivity is equal to $D_{\mathrm{CH_4,air}}$.

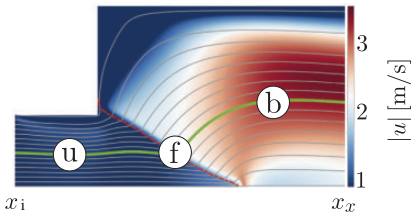

Figure 12. Velocity field from the steady state computational fluid dynamics simulation (Pe = 450) with a highlighted streamline (——). The unburned region is denoted by 'u', the burned one by 'b' and the flame front by 'f'.

We evaluate the aforementioned 1D model on each streamline by combining two regions, one containing burned and one unburned fluid, in a row. Each region is characterised by an averaged flow velocity and an averaged diffusion coefficient. In doing so, each of the N evaluated streamlines yields an ETF of its own. For the setup shown in Figure 12 some examples of those individual transfer functions are plotted in Figure 13 (grey lines) in terms of IR and FR. Due to wall friction, streamlines close to the wall exhibit a larger time delay than those close to the centre line. Hence, their IR is delayed and more spread out. This corresponds to a lower cut-off frequency of the FR and to a steeper slope of the phase. The inclined flame also affects the mean time delays of the computed ETFs. Fluid particles on a central streamline are exposed to the unburned slow flow for a longer time than particles on a line further outside. The opposite holds for the burned fast flow. While all transfer functions are different, they only vary within a relative narrowly bounded region.

In order to get the overall ETF of the configuration, we connect all N individual streamline transfer functions in parallel and weight each by the associated portion of the total volume flux. These weights are computed from

$$w_i = \left.\frac{\bar{u}_{\mathrm{SL},i} A_i}{\dot{V}}\right|_{x_x}, \tag{28}$$

where $\bar{u}_{\mathrm{SL},i}$ denotes the streamline aligned velocity at the outlet reference position and A_i the cross sectional area of the associated flow channel of the i-th streamline. The total volume flux is indicated by $\dot{V}$. The resulting ETF, using 51 streamlines, is plotted in Figure 13 (-·-·-). Very similar results are already achieved by using only 10 streamlines. The overall impact of a few

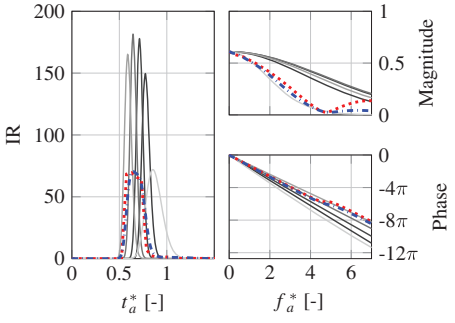

Figure 13. Entropy transfer function E_ϕ for the Pe = 450 setup plotted in the time (left) and the frequency domain (right). N1D advection-diffusion model: The grey lines show the entropy transfer function for some individual streamlines. Bright to dark line colours correspond to outer to inner radii. The resulting distribution is plotted as (-·-·-). Additionally, results for neglected diffusion (advection only) are shown as: (-·-·-).

streamlines that exhibit a large time delay in their IR is quite low. This can be explained by the fact that they are positioned close to the combustor wall and, hence, only carry a small portion of the total volume flux. Thus, their corresponding weighting factors are insignificant. The overall IR is generally more spread out than the individual ones. This directly translates to a lower cut-off frequency of their FR. The overall phase is essentially influenced by the fastest flow channels (low slope) since they are responsible for most of the volume flux.

This result demonstrates the effect of advective dispersion as a 2D/3D effect. The superposition of the individual streamline transfer functions, which all exhibits a slightly different mean time delay, leads to a spreading out and, hence, a dispersion of the overall ETF. This effect is present even without diffusive effects. In order to emphasise this, we now solve the individual streamline ETFs by neglecting diffusion. This corresponds to setting $D(x_1, t) = \delta(x_1)$ in equation (21). Instead of using the average velocity, we now use the local streamline aligned velocity, which is a function of the streamline aligned coordinate x_{SL}. The time delay of the i-th streamline is then computed by

$$\tau_i = \int_{x_i}^{x_x} \frac{1}{|\bar{u}_{\mathrm{SL}}(x_{\mathrm{SL}})|} \mathrm{d}x_{\mathrm{SL}}. \tag{29}$$

An IR which consists of one spike at the time delay τ_i is obtained for each individual ETF. The overall ETF, which is retrieved from this model, is plotted in Figure 13 (-·-·-) and agrees well with the previous advection diffusion model. In this specific case, diffusion plays only a minor role. The spreading out of the IR is mainly attributed to advective dispersion. This is different for the $\mathrm{Pe} = 90$ case, as it will be shown in section 6. It should be pointed out that the ETF model proposed by Wassmer et al.[26] respected both diffusion and advective dispersion by using an effective diffusivity, which mimics the combined effect. Its value was retrieved by a fit to experimental data.

Due to the fact that N 1D models are connected in parallel, we call the overall model 'N1D'. The instant respecting advection and diffusion is called 'N1D-AD' and the one respecting only advection 'N1D-A' model in the following. A validation of these models using data from CFD simulations is presented in section 6.

5.3. State space model

The N1D model provides a method that allows us to gain important physical insights into the processes governing the response to equivalence ratio fluctuations. The effect of advective dispersion can be separated and it is shown that even the inclusion of a combustion zone does not alter the way of modelling the overall transfer function for mixture fraction compared to a cold flow inside a duct. The dynamics can be captured well by connecting N 1D ducts in parallel. This knowledge also allows us to perform quick analytical estimates of the ETF by choosing one or two representative streamlines, estimate the advection velocity and deduce from them the rough shape of the ETF.

In the following, we want to introduce a method which requires less modelling than the N1D model. Hence, its application is simpler and more general. We follow an idea outlined by van Kampen et al.,[48] who argued that the steady state results of a CFD simulation, together with the knowledge of the equations which were solved by the simulation, are sufficient to determine the linear behaviour of the system. Both the FTF and the ETF describe how a system responds to small perturbations, i.e. reflect its linear response to input fluctuations of certain quantities. Thus, those functions can directly be computed from the linear representation of the investigated system without the need of an expensive transient simulation of the original, non-linear system.

The steady state CFD data for the current setups were already presented in section 3.2. The linear equation which governs the transport process for adiabatic conditions is derived in Appendix 2 and is an advection diffusion equation. As shown in section 5.1, it can be transformed to an equation for the normalised mixture fraction fluctuation Ξ which reads

$$\bar{\rho}\frac{\partial \Xi}{\partial t} + \bar{\rho}\bar{u}_i\frac{\partial \Xi}{\partial x_i} = \frac{\partial}{\partial x_i}\left(\bar{\rho}D_f\frac{\partial \Xi}{\partial x_i}\right). \tag{30}$$

The steady state velocity field $\bar{u}_i$ and the density $\bar{\rho}$ are retrieved from the steady state CFD data. The diffusion coefficient D_f is again computed from the temperature field using the Chapman–Enskog theory. This equation is then discretised by using the Finite Elements (FE) approach with Lagrangian shape functions of quadratic order. A triangular mesh with a refined region at the edges of about 100 elements for the $\mathrm{Pe} = 90$ and 300 elements for the $\mathrm{Pe} = 450$ cases is used. The mesh independence of the solution was checked for both cases. Hence, comparatively few elements are required in order to get a good estimate of the transfer function. An SS representation of the PDE from equation (30) of the form

$$\dot{\Xi}(t) = A\,\Xi(t) + B\phi'\big|_{x_i} \tag{31}$$

$$\left.\frac{T'(t)}{\bar{T}}\right|_{x_x} = C\Xi(t) \tag{32}$$

is generated. This system is defined by three matrices: Matrix A is determined by the spatial FE discretisation and is only sparsely filled. Matrix B contains the information about which states of $\Xi(t)$ are excited by the input signal $\phi'|_{x_i}$. Hence, the transformation from equivalence ratio to mixture fraction, provided by equation (17) needs to be included into this matrix. The output of the system is the mass flux averaged temperature fluctuation at the domain outlet. For this purpose, probes have to be defined, which set the structure of the matrix C. The present study uses the COMSOL Multiphysics® tool to build the SS systems.

The ETF can now be computed directly from the SS system represented by equations (31) and (32)

$$E_\phi(\omega) = C(\omega I - A)^{-1}B. \tag{33}$$

for each angular frequency ω of interest. Thus, one linear system per sample point of the FR has to be solved. Using harmonic excitation in the time domain would be much more expensive. Note that the FRs presented in section 6 are computed from equation (33). The IRs, on the other hand, are evaluated as the time derivative of the step responses (computed in time domain).

In order to visualise the dynamics of the model, we integrate the SS system of the Pe = 450 setup in time using a unit step as an input signal. Six snapshots of this simulation are plotted in Figure 14. The relative fluctuation of equivalence ratio is increased from zero to unity at $t = 0$. This translates to a rise of the relative mixture fraction from zero to $\Xi = 0.955$. This perturbation (coloured in red) is then convected from the inlet of the domain towards the flame front, where it is visibly accelerated inside the burned flow domain. Also, the increase of the diffusion coefficient becomes noticeable here. In the fifth snapshot, the perturbation reaches the reference plane at x_x and a new steady state is about to be established.

6. Validation

All proposed models are now validated against the CFD/SI results presented in section 3.3. For that purpose, IRs as well as their FRs are compared. The results are shown in Figures 15 and 16 for the Pe = 90 and the Pe = 450 setup, respectively. All proposed models yield good predictions of the ETF. The only exception is the implementation of the N1D-A model for the Pe = 90 case. Here, the neglect of diffusion leads to a significant underestimation of dispersive effects on the IR. Nevertheless, the phase behaviour is captured well.

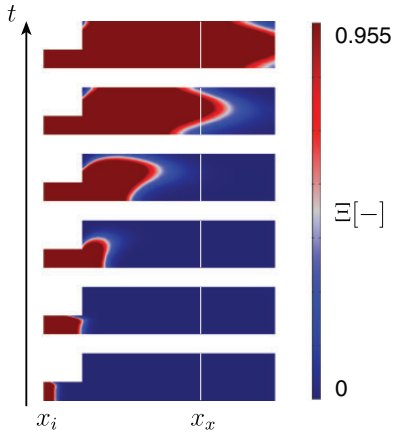

Figure 14. Snapshots of a unit step response of the state space system given by equations (31) and (32) for the Pe = 450 case. The time interval between two snapshots equals 6 ms.

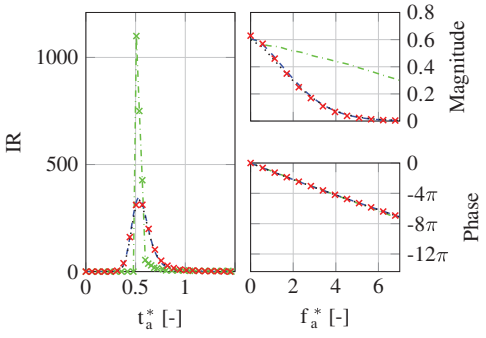

Figure 15. Entropy transfer function E_ϕ for the Pe = 90 setup plotted in the time (left) and the frequency domain (right). Computational fluid dynamics/system identification (× × ×); state space model (·····); N1D-advection-diffusion model (- - - -); N1D-A model (-·-·-).

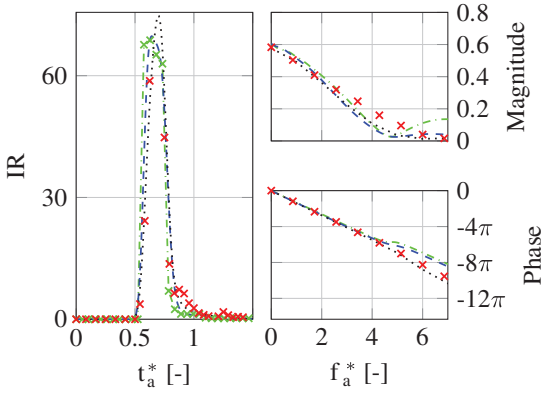

Figure 16. Entropy transfer function E_ϕ for the Pe = 450 setup plotted in the time (left) and the frequency domain (right). Computational fluid dynamics/system identification (× × ×); state space model (·····); N1D-advection-diffusion model (- - - -); N1D-A model (-·-·-).

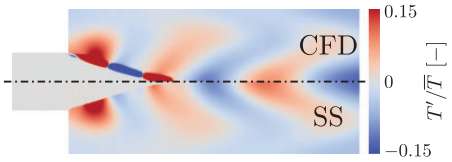

Figure 17. Snapshots of relative temperature fluctuations for the Pe = 450 setup taken from a computational fluid dynamics and a state space simulation subjected to a broad band equivalence ratio forcing, as described in section 3.3.

For the Pe = 450 setup, the influence of diffusion is considerably less pronounced. As expected, diffusion is especially relevant for the low Péclet number case and, thus, the N1D-A model should only be used for sufficiently high Péclet numbers.

Comparing snapshots of the CFD simulation with broad band equivalence ratio forcing and the SS model, good agreement can be found. This is shown for one instant in time in Figure 17: The upper half shows the normalised temperature fluctuations for the CFD simulation, the lower half for the SS model. The strong perturbations at the flame front present in the CFD results are caused by (small) movements of the flame which are inherently neglected by the SS model. Downstream of the flame, very good agreement between both models is achieved. Due to the nature of the used broad band signal, which modulates the incoming equivalence ratio, the applied forcing amplitude varies over time. Hence the relative temperature fluctuations for the snapshot shown are within the range of ±0.15. This might increase/decrease for other times.

7. Range of validity

Since the two provided test case setups are very specific and of rather academic nature, one may wonder what the expected range of validity of the proposed modelling approaches is. In the following we discuss the validity of the models for setups of practical relevance.

Many combustion systems use fuels other than pure methane. Although the structure of the combustion model introduced with equation (15) is formulated for lean methane-air mixtures, it is not limited to this type of fuel. The model may be applied to different types of fuel without essential modification, provided that the chemical time scales are short compared to the time scales of upstream equivalence ratio fluctuations and that the combustion process is lean. In order to derive the static gain for different fuels, good models for the respective dependency of the specific heat of the unburned/burned products on mean equivalence ratio are required.

An important constraint for the presented models is the use of adiabatic boundary conditions. Due to the high temperature of the combustion products, significant heat losses inside the combustion chamber should be expected. They lead, on the one hand, to a reduction of the oscillation amplitude of temperature fluctuations. On the other hand, they could lead to the generation of additional temperature inhomogeneities at cooled walls. Assessing the discussed models for non-adiabatic boundary conditions should hence be subject of further investigations.

Following Hussain and Reynolds,[49] a general transient velocity field u can be decomposed into a temporal mean $\bar{u}$ and into a deterministic (coherent structures $\tilde{u}$) as well as a stochastic fluctuation (turbulence u')

$$u(x,t) = \bar{u}(x) + \tilde{u}(x,t) + u'(x,t). \tag{34}$$

Strictly speaking, all transport models derived within this paper are only valid if neither deterministic nor stochastic fluctuations are present in the unforced flow and if, additionally, no significant velocity fluctuations are caused by upstream equivalence ratio fluctuations or their effects (e.g. by a change in heat release). Morgans et al.[38] showed that effects of turbulence are small compared to those related to mean flow gradients (advective dispersion). Hence, the influence of turbulent dispersion should be negligible or – if that is not so – can be modelled to a straightforward way by a turbulent diffusivity. Concerning large scale coherent structures caused, for example, by shear layer instabilities, Xia et al.[50] found that they may lead to significant additional dispersion of the IR and hence to a lower cut-off frequency of the transfer function. In this regard, the proposed models can only serve as a first estimate of the ETF. Most combustors of practical relevance use swirl stabilised flames. Since for such configurations the velocity field contributes to all three components of equation (34) further studies about the predictive quality of the proposed models have to be performed.

The mixing of combustion products with dilution air is another important source of entropy waves (see e.g. Motheau et al.[51] or Livebardon et al.[52]). The models for the generation of temperature inhomogeneities proposed in this paper are formulated in terms of mixture fraction, thus in principle they should be capable of describing entropy waves resulting from such mixing processes with quantitative accuracy.

8. Summary and conclusions

The transfer function from equivalence ratio upstream of a flame to temperature fluctuations downstream of a flame has been analysed and modelled. For that reason, transient high fidelity CFD simulations of two laminar premixed flames were performed and the desired response functions were estimated from the simulation

data by means of SI (CFD/SI). These results served as a validation basis.

It was shown that the overall problem can be subdivided into two sub-problems: (1) the transformation of equivalence ratio to temperature at the flame and (2) the transport processes for mixture fraction. The first was modelled by assuming an FRZ, which immediately transforms upstream equivalence ratio to downstream temperature fluctuations. It can, therefore, be expressed by a static gain, which is a function of the mean equivalence ratio. Problem (2) reduces for the assumptions made to a convection problem, which can be solved independently of the combustion problem (1).

The transport problem was solved by two models: firstly a semi-analytical 'N1D'-model, and secondly a finite-element-based state space model. Both models rely on mean field data provided by CFD simulation. The N1D model captures the 2D transport process as a superposition of a number N of 1-dimensional models, which represent the evolution along respective streamlines. Respecting both diffusion and advection gave us a model called N1D-AD, considering only advection one called N1D-A. The latter variant was used to show that diffusive processes are only relevant for high Péclet numbers. On the other hand, state space model is based on a discretised 2D partial differential equation and, hence, needs to be solved numerically. An state space system is constructed using a Finite Element approach, which may be solved in frequency or time domain. Both proposed models showed good agreement with CFD/SI results.

The main findings of the present analysis are:

1. The entropy response function exhibit dynamics that differ essentially from the response function for heat release rate. Hence, fluctuations of global heat release should not be used to model the generation of entropy waves.
2. Modelling the ETF for adiabatic conditions and a stationary base flow field with $\mathrm{Le} \approx 1$ requires two sub-models: One for the transformation of equivalence ratio to temperature fluctuations and one for the advective and diffusive transport processes.
3. The transformation $\phi'/\bar{\phi} \rightarrow T'/\bar{T}$ at the flame front is well captured by an FRZ model and may be described by a static gain $\vartheta_{\mathrm{FRZ}}(\bar{\phi})$.
4. For modelling the static gain ϑ_{FRZ}, variations of the heat of reaction Δh_R, the temperature of the burned fluid *and* the specific heat capacity c_p of the mixture need to be taken into account. Neglecting the latter leads to a significant overestimation of temperature inhomogeneities that result from fluctuations of the equivalence ratio. At near-stoichiometric conditions an additional empirical term is required, which captures the reduced production of entropy waves due to incomplete conversion of reactants to products.
5. Transport processes may be described by the convection of mixture fraction. For high Péclet numbers advection is dominant.
6. Advective dispersion is a 2D/3D feature that leads to significant spreading of the IR and, thus, to a reduction of the cut-off frequency.

Acknowledgements

The authors thank the Leibniz Supercomputing Centre for access to its cluster system.

Declaration of Conflicting Interests

The author(s) declared no potential conflicts of interest with respect to the research, authorship and/or publication of this article.

Funding

The author(s) received no financial support for the research, authorship and/or publication of this article.

References

1. Culick FEC. In: Culick F, Heitor MV and Whitelaw JH (eds) *Unsteady combustion, volume 306 of NATO ASI series, series E: applied sciences*, 1st ed. Netherlands: Springer, 1996, pp.173–241.
2. Candel S, Durox D, Ducruix S, et al. Flame dynamics and combustion noise: progress and challenges. *Int J Aeroacoustics* 2009; 8: 1–56.
3. Poinsot T. Prediction and control of combustion instabilities in real engines. *Proc Combus Inst* 2017; 36: 1–28.
4. Schuermans BBH, Polifke W, Paschereit CO, et al. Prediction of acoustic pressure spectra in combustion systems using swirl stabilized gas turbine burners. In: *IGTI TE2000*, ASME 2000-GT-105. Munich, Germany, 2000.
5. Dowling AP and Mahmoudi Y. Combustion noise. *Proc Combust Inst* 2015; 35: 65–100.
6. Silva CF, Merk M, Komarek T, et al. The contribution of intrinsic thermoacoustic feedback to combustion noise and resonances of a confined turbulent premixed flame. *Combust Flame* 2017; 182: 269–278.
7. Ihme M. Combustion and engine-core noise. *Annu Rev Fluid Mech* 2017; 49.
8. Marble FE and Candel SM. Acoustic disturbance from gas non-uniformities convected through a nozzle. *J Sound Vib* 1977; 55: 225–243.
9. Duran I and Moreau S. Solution of the quasi-one-dimensional linearized Euler equations using flow invariants and the Magnus expansion. *J Fluid Mech* 2013; 723: 190–231.
10. Leyko M, Nicoud F and Poinsot T. Comparison of direct and indirect combustion noise mechanisms in a model combustor. *AIAA J* 2009; 47: 2709–2716.
11. Morgans AS and Duran I. Entropy noise: a review of theory, progress and challenges. *Int J Spray Combust Dyn* 2016; 8: 285–298.

12. Magri L, O'Brien J and Ihme M. Compositional inhomogeneities as a source of indirect combustion noise. *J Fluid Mech* 2016; 799: R4.
13. O'Brien JD and Ihme M. Species dependency of the compositional indirect noise mechanism. In: *Proceedings of ASME turbo expo 2017: turbomachinery technical conference and exposition*, volume GT2017-63076. Charlotte, NC, USA, 2017.
14. Cumpsty NA. Jet engine combustion noise: pressure, entropy and vorticity perturbations produced by unsteady combustion or heat addition. *J Sound Vib* 1979; 66: 527–544.
15. Li L and Sun X. Effect of vorticity waves on azimuthal instabilities in annular chambers. *Combust Flame* 2015; 162: 628–641.
16. Keller JJ, Egli W and Hellat J. Thermally induced low-frequency oscillations. *Z Für Angew Math Phys ZAMP* 1985; 36: 250–274.
17. Polifke W, Paschereit CO and Döbbeling K. Constructive and destructive interference of acoustic and entropy waves in a premixed combustor with a choked exit. *Int J Acoust Vib* 2001a; 6: 135–146.
18. Sattelmayer T. Influence of the combustor aerodynamics on combustion instabilities from equivalence ratio fluctuations. *J Eng Gas Turbines Power* 2003; 125: 11–19.
19. Dowling AP and Stow SR. Acoustic analysis of gas turbine combustors. *J Propuls Power* 2003; 19: 751–764.
20. Goh CS and Morgans AS. The influence of entropy waves on the thermoacoustic stability of a model combustor. *Combust Sci Technol* 2013; 185: 249–268.
21. Schulz O and Noiray N. Autoignition Flame Dynamics in Sequential Combustors. Presented at the International Symposium Thermoacoustic Instabilities in Gas Turbines and Rocket Engines, ETH-Zürich, Munich, Germany 2017. doi: 10.3929/ethz-a-010819327.
22. Dowling AP. The calculation of thermoacoustic oscillation. *J Sound Vib* 1995; 180: 557–581.
23. Hield PA, Brear MJ and Jin SH. Thermoacoustic limit cycles in a premixed laboratory combustor with open and choked exits. *Combust Flame* 2009; 156: 1683–1697.
24. Strobio Chen L, Bomberg S and Polifke W. Propagation and generation of acoustic and entropy waves across a moving flame front. *Combust Flame* 2016a; 166: 170–180.
25. Strobio Chen L, Steinbacher T, Silva C, et al. On generation of entropy waves across a premixed flame. In: *Proceedings of ASME 2016 turbo expo: turbomachinery technical conference & exposition*, GT2016-57026. Seoul, Korea, 2016b.
26. Wassmer D, Schuermans B, Paschereit CO and Moeck JP. Measurement and Modeling of the Generation and the Transport of Entropy Waves in a Model Gas Turbine Combustor. *International Journal of Spray and Combustion Dynamics* 2017; doi: 10.1177/1756827717696326.
27. Polifke W. Black-box system identification for reduced order model construction. *Ann Nucl Energy* 2014; 67C: 109–128.
28. Chu BT and Kovasznay LSG. Non-linear interactions in a viscous heat-conducting compressible gas. *J Fluid Mech* 1957; 3: 495–514.
29. Cumpsty NA, Nicholas A and Marble FE. The generation of noise by the fluctuations in gas temperature into a turbine. Technical Report CUED/A TURBO/TR57, Cambridge, England, 1974.
30. Lieuwen T. Modeling premixed combustion – Acoustic wave interactions: a review. *J Propuls Power* 2003; 19: 765–781.
31. Cho JH and Lieuwen TC. Laminar premixed flame response to equivalence ratio oscillations. *Combust Flame* 2005; 140: 116–129.
32. Huber A and Polifke W. Dynamics of practical premix flames, part I: model structure and identification. *Int J Spray Comb Dyn* 2009; 1: 199–228.
33. The OpenFOAM Foundation. OpenFOAM 2.3.1, https://openfoam.org/.
34. Bibrzycki J, Poinsot T, and Zajdel, A. Investigation of Laminar Flame Speed of $Ch_4/N_2/O_2$ and $Ch_4/Co_2/O_2$ Mixtures Using Reduced Chemical Kinetic Mechanisms. *Archivum combustionis* 2010; 30(4): 287–296.
35. Duchaine F, Boudy F, Durox D, et al. Sensitivity analysis of transfer functions of laminar flames. *Combust Flame* 2011; 158: 2384–2394.
36. Jaensch S, Merk M, Gopalakrishnan E, et al. Hybrid CFD/low-order modeling of nonlinear thermoacoustic oscillations. In: *36th Int'l symposium on combustion*. Seoul, Korea, 2016.
37. Polifke W, Kopitz J and Serbanovic A. Impact of the fuel time lag distribution in elliptical premix nozzles on combustion stability. In: *7th AIAA/CEAS aeroacoustics conference*, AIAA 2001-2104. Maastricht, The Netherlands, 2001b.
38. Morgans AS, Goh CS and Dahan JA. The dissipation and shear dispersion of entropy waves in combustor thermoacoustics. *J Fluid Mech* 2013; 733.
39. Föller S and Polifke W. Advances in identification techniques for aero-acoustic scattering coefficients from large eddy simulation. In: *18th International Congress on Sound and Vibration (ICSV18)*, volume 4. Rio de Janeiro, Brazil, 2011, pp.3122–3129.
40. Jaensch S, Emmert T, Silva CF, et al. A Grey-box identification approach for thermoacoustic network models. In: *Proceedings of ASME turbo expo*, GT2014-27034. Düsseldorf, Germany, 2014.
41. Blumenthal RS, Subramanian P, Sujith R, et al. Novel perspectives on the dynamics of premixed flames. *Combust Flame* 2013; 160: 1215–1224.
42. Albayrak A, Blumenthal RS, Ulhaq A, et al. An analytical model for the impulse response of laminar premixed flames to equivalence ratio perturbations. In: *36th int'l symposium on combustion*. Combustion Institute, 2016.
43. Goodwin DG, Moffat HK and Speth RL. *Cantera: an object-oriented software toolkit for chemical kinetics, thermodynamics, and transport processes, Version 2.2.1*, www.cantera.org (accessed 1 December 2016).
44. Smith GP, Golden DM, Frenklach M, et al. *GRI-Mech 3.0*, www.me.berkeley.edu/gri_mech (accessed 10 November 2016).
45. Abu-Off G and Cant R. Reaction rate modeling for premixed turbulent methane-air flames. In: *Proceedings of the Joint Meeting of Spanish, Portuguese, Swedish and British sections of the Combustion Institute*. Madeira, 1996.

46. Bilger RW. Turbulent diffusion flames. *Annu Rev Fluid Mech* 1989; 21: 101–135.
47. Poling BE, Prausnitz JM and O'Connell JP. Chapter 11-3: diffusion coefficients for binary gas systems at low pressures: prediction from theory. In: *The properties of gases and liquids*. 5th ed. McGraw-Hill, 2001.
48. van Kampen JF, Kok JBW and van der Meer TH. Efficient retrieval of the thermo-acoustic flame transfer function from a linearized CFD simulation of a turbulent flame. *Int J Numer Meth Fluids* 2007; 54: 1131–1149.
49. Hussain AKMF and Reynolds WC. The mechanics of an organized wave in turbulent shear flow. *J Fluid Mech* 1970; 41: 241–258.
50. Xia Y, Duran I, Morgans AS, et al. Dispersion of entropy waves advecting through combustor chambers. In: *23rd international congress on sound & vibration*. Athens, Greece, 2016.
51. Motheau E, Nicoud F and Poinsot T. Mixed acoustic–entropy combustion instabilities in gas turbines. *J Fluid Mech* 2014; 749: 542–576.
52. Livebardon T, Moreau S, Gicquel L, et al. Combining les of combustion chamber and an actuator disk theory to predict combustion noise in a helicopter engine. *Combust Flame* 2016; 165: 272–287.
53. Lieuwen TC. Chapter 1: overview and basic equations. In: *Unsteady combustor physics*. Vol 1, Cambridge: Cambridge University Press, 2012, pp.1–16.

Appendix 1. Empirical terms for the FRZ model

Deriving equation (13) in section 4 an integral appears which is rewritten in terms of a function I_{c_p}

$$I_{c_p} = \frac{1}{\left(\bar{T}_b - \bar{T}_u\right)} \int_{\bar{T}_u}^{\bar{T}_b} \left.\frac{\partial c_p\left(\tilde{T}, \phi\right)}{\partial \phi}\right|_{\bar{\phi}_u} \mathrm{d}\tilde{T}. \tag{35}$$

Since the integrand, which is the gradient of c_p with respect to the equivalence ratio evaluated at $\phi_u = \bar{\phi}_u$, can in practice only be assessed at the unburned and the burned state, we employ the trapezoidal rule in order to approximate the integral

$$I_{c_p} \approx \frac{1}{2}\left[\left.\frac{\partial c_p\left(\bar{T}_u, \phi\right)}{\partial \phi}\right|_{\bar{\phi}_u} + \left.\frac{\partial c_p\left(\bar{T}_b, \phi\right)}{\partial \phi}\right|_{\bar{\phi}_u}\right]. \tag{36}$$

Both gradients appearing here can be estimated for lean methane-air flames by employing the numerical Cantera model described in section 4.1. Evaluating the specific heat capacity for the unburned and the burned fluid for a range of equivalence ratios results in two curves, which are plotted in Figure 18 (middle and bottom). Fitting linear functions $c_{p,b/u}^{\mathrm{fit}}$ in the interval $0.6 \leq \phi \leq 0.8$ to those curves, yields the desired gradients. We retain $\mathrm{d}c_{p,b}^{\mathrm{fit}}/\mathrm{d}\phi \approx 402.9\mathrm{J/kg/K}$ and $\mathrm{d}c_{p,u}^{\mathrm{fit}}/\mathrm{d}\phi \approx 65.7\mathrm{J/kg/K}$ for the slopes of the specific heat capacities. This results in

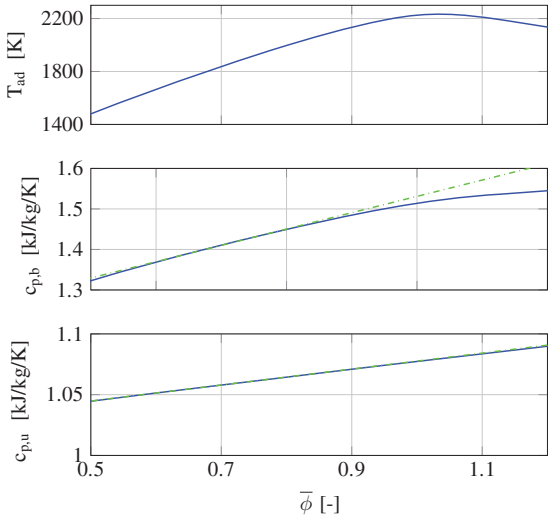

Figure 18. Adiabatic flame temperature T_{ad} (top), specific heat capacity of the burned c_{pb} (——, middle) and the unburned fluid c_{pu} (——, bottom) over equivalence ratio for constant pressure. Linear fit to c_{pb} and c_{pu} in the range $0.5 \leq \bar{\phi} \leq 0.8$ (- - - -, middle and bottom).

$$I_{c_p} = 234.3\mathrm{J/kg/K}. \tag{37}$$

The second empirical term is the $C_{\mathrm{inc}}(\phi)$ term of equation (15). It respects the effects of incomplete combustion close to stoichiometric conditions which leads to a non-linear behaviour of the adiabatic flame temperature in this region as it can be seen in Figure 18 (top). The values for T_{ad} shown here are also computed using the aforementioned Cantera model. Based on the observation that the discrepancy between the analytical model of equation (14) and the numerical data exponentially increases with the equivalence ratio, starting from zero at $\bar{\phi}_u \approx 0.8$, we propose an exponential term

$$C_{\mathrm{inc}}(\phi) = c_1 \exp(c_2 \phi) \tag{38}$$

as basis for the empirical model. By minimising the difference of the static gain between the advanced model of equation (15) and the reference one (——, Figure 8) for $0.75 < \bar{\phi} < 1.05$, the two constants can be estimated to $c_1 = 7.377e-7$ and $c_2 = 13.21$. The resulting term is shown over the mean equivalence ratio in Figure 19. It only contributes to mixtures with equivalence ratios of $\bar{\phi} \gtrsim 0.8$.

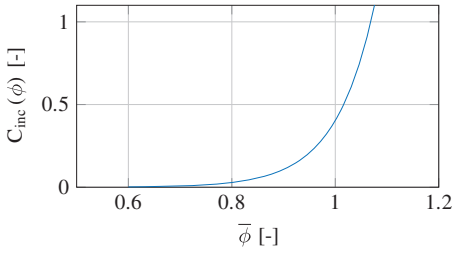

Figure 19. Empirical term respecting incomplete combustion at stoichiometric conditions from equation (38) plotted over mean equivalence ratio.

Appendix 2. Simplified transport equation for enthalpy

The energy equation for an isobaric fluid with neglected viscous dissipation and body forces reads

$$\rho\frac{Dh}{Dt} = \rho\frac{\partial h}{\partial t} + \rho u_i\frac{\partial h}{\partial x_i} = \frac{\partial}{\partial x_i}\left(\lambda\frac{\partial T}{\partial x_i}\right) + \frac{\partial}{\partial x_i}\left(\rho\sum_{k=1}^{N} h_k D_k\frac{\partial y_k}{\partial x_i}\right) \tag{39}$$

(see e.g. Lieuwen[53]). Here Soret thermodiffusion, pressure and body force terms are neglected and binary diffusion was assumed. The thermal conductivity is denoted by λ, the density by ρ, the enthalpy and the diffusion coefficient of the k-th species in air by h_k and D_k respectively. The number of species is N with each quantified by a mass fraction y_k. The Einstein notation is employed for all spatial derivatives. The total enthalpy h along a streamline is therefore affected by thermal diffusion and by mass transport due to molecular diffusion of the species. For low Mach numbers, it can be decomposed into a chemical h_c and a sensible h_s enthalpy. From the species conservation equation, a transport equation for the chemical enthalpy can be derived

$$\rho\frac{Dh_c}{Dt} = \frac{\partial}{\partial x_i}\left(\rho\sum_{k=1}^{N} h^0_{f,k} D_k\frac{\partial y_k}{\partial x_i}\right) + \sum_{k=1}^{N} h^0_{f,k}\dot{\omega}_k \tag{40}$$

with the standard enthalpy of formation $h^0_{f,k}$ of the k-th species and the species production/consumption rate $\dot{\omega}_k$. For an inlet temperature at standard conditions (usually $T_{st} = 298.15\text{K}$ and $p_{st} = 1\text{bar}$) and lean combustion, locally, all chemical enthalpy which can potentially be transformed to sensible enthalpy is specified by the LHV H_l and the mass fraction of methane y_{CH4}. Thus, we can write for the chemical enthalpy $h_c = y_{CH4} H_l$ and need therefore only to track the mass fraction of y_{CH4}. The equation for the chemical enthalpy can hence be transformed to

$$\rho\frac{Dh_c}{Dt} = \frac{\partial}{\partial x_i}\left(\rho D_{CH4,\,air}\, H_l\frac{\partial y_{CH4}}{\partial x_i}\right) + H_l\, y_{CH4}\,\dot{\omega}. \tag{41}$$

Subtracting equation (40) from the equation for the total enthalpy equation (39) yields a formula for the sensible enthalpy

$$\rho\frac{Dh_s}{Dt} = \frac{\partial}{\partial x_i}\left(\lambda\frac{\partial T}{\partial x_i} + \rho\sum_{k=1}^{N} D_k h_{s,k}\frac{\partial y_k}{\partial x_i}\right) - H_l\, y_{CH4}\,\dot{\omega}. \tag{42}$$

Comparing equations (39), (41) and (42) one notices that a sink of chemical enthalpy is a source of sensible enthalpy. For the total enthalpy these source terms cancel each other out so that it is neither produced nor consumed. Chemical enthalpy is diffused due to gradients in y_{CH4}, the sensible counterpart due to temperature *and* species mass fraction gradients.

The temperature term in equation (42) can be rewritten by using the relation $\mathrm{d}h_s = c_p\mathrm{d}T + \sum_{k=1}^{N} h_{s,k}\mathrm{d}y_k$. Introducing the species Lewis number $\mathrm{Le}_k = \lambda/(\rho c_p D_k)$ equation (42) now reads

$$\rho\frac{\mathrm{D}h_s}{\mathrm{D}t} = \frac{\partial}{\partial x_i}\left[\frac{\lambda}{c_p}\frac{\partial h_s}{\partial x_i} + \frac{\lambda}{c_p}\sum_{k=1}^{N} h_{s,k}\frac{\partial y_k}{\partial x_i}\left(\frac{1}{\mathrm{Le}_k} - 1\right)\right] - H_l\, y_{CH4}\,\dot{\omega}. \tag{43}$$

If we now, additionally, assume that the Lewis numbers for all species are unity, which is a reasonable approximation for methane air flames, this equation is further simplified to

$$\rho\frac{\mathrm{D}h_s}{\mathrm{D}t} = \frac{\partial}{\partial x_i}\left(\rho D_f\frac{\partial h_s}{\partial x_i}\right) - H_l\, y_{CH4}\,\dot{\omega} \tag{44}$$

where a diffusion coefficient D_f is introduced which is common for all molecular and thermal diffusion processes. The assumption of equal diffusivities for all species is in particular a good approximation for turbulent flows where the turbulent convection can be modelled as an enhanced diffusion coefficient. Since this contributes to the molecular diffusivities for all species as well as to the diffusion of heat, with increasing turbulence the $\mathrm{Le} = 1$ assumption becomes better for all kinds of fuels. Adding the equation for the chemical enthalpy (41) to the one for the sensible

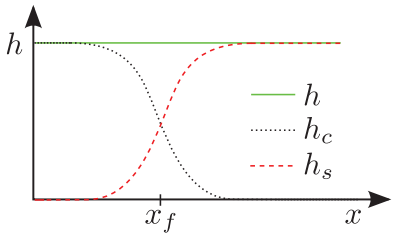

Figure 20. Schematic plot of the total enthalpy h (——), the chemical enthalpy h_c (·····) and the sensible enthalpy h_s (- - -) normal through a flame which is placed at $x = x_f$ for Le = 1.

enthalpy (44), we get an expression for the total enthalpy

$$\rho \frac{Dh}{Dt} = \frac{\partial}{\partial x_i}\left(\rho D_f \frac{\partial h_s}{\partial x_i} + \rho D_f \frac{\partial h_c}{\partial x_i}\right). \tag{45}$$

The diffusion coefficient of methane in air is again replaced by D_f and the LHV H_l and the mass fraction of methane y_{CH4} are combined to h_c. If we also assume adiabatic boundaries, the boundary conditions of h_c and h_s coincide and, thus, we can write

$$\rho \frac{Dh}{Dt} = \frac{\partial}{\partial x_i}\left(\rho D_f \frac{\partial h}{\partial x_i}\right). \tag{46}$$

For the adiabatic cases, the relation of the three types of enthalpy along a path x normal through a flame are illustrated in Figure 20. The chemical enthalpy decreases when approaching the flame position x_f while the sensible enthalpy is rising at the same time. Both combined yield a constant total enthalpy. Note that the Le = 1 assumption is important for the absence of spatial gradients of the total enthalpy. If the boundaries were diabatic, this would lead to a loss of sensible, and hence also total, enthalpy in the burnt part of the fluid.